Combining Densification and Coarsening in a Cellular Automata-Monte-Carlo Simulation of Sintering: Methodology and Calibration

Xin Wang and Alan Atkinson

Department of Materials, Imperial College London SW7 2BP, UK

Abstract

A hybrid Cellular Automata-Monte Carlo (CA-MC) approach is developed to simulate the sintering of particulate materials. The approach embodies a new, and physically realistic, way of simulating densification by grain boundary diffusion and collapse that takes into account the stresses arising from interactions with neighbouring particles (grains) by minimising the stored energy and energy dissipation rate using the variational principle. The parameters in the CA-MC simulations are calibrated in terms of measurable physical quantities by simulating the sintering of two identical contacting spheres, for which analytical solutions are well known and widely accepted. The use of the model is illustrated by simulating the densification of a randomly packed assembly of spherical particles. This demonstrates that the interactions between particles significantly inhibits shrinkage compared with that of two isolated spheres.

Key words: Sintering, Densification, Modelling, Microstructure evolution, Cellular automata, Monte-Carlo

1 Introduction

Sintering of assemblies of particulates (such as powder compacts) involves both coarsening and densification driven by the excess energy of solid/pore interfaces. Surface diffusion, from positions of high curvature to positions of low curvature, leads to coarsening without densification. In crystalline materials densification is caused by diffusion from grain boundaries to positions of low curvature and subsequent collapse (annihilation of vacancies) at the grain boundary bringing the grain centres closer together. Theoretical modelling plays an important role in improving understanding of the sintering process. Originally, sintering theory concentrated on simple two-sphere models [1-5] with one neck formed between two identical spherical particles. Despite the simplification, these models were successful in providing

fundamental understanding about the sintering driving force and the transport processes controlling the kinetics of neck growth and shrinkage.

The initial morphology and topological features of real microstructures, and their evolution during sintering are much more complicated than is assumed in most simulation methods described in the literature. For example, it has been observed experimentally [6] that the faceted surfaces of particles can lead to neck growth kinetics that are significantly different from the predictions of classic continuum theory (which is based on idealised spherical particles). Therefore there is a clear need to include the evolution of more realistic microstructural features during the simulation of sintering [7].

Although useful for fundamental insight, two-sphere models cannot describe the macroscopic behaviour of a typical powder compact, in which multi-particle interaction occurs, involving thousands to millions of particles having different shapes, sizes and arrangements. To try and tackle this, micromechanical models [5, 8, 9] based on periodic unit cells were developed, which described the macroscopic viscous behaviour of a powder compact based on information such as starting particle size and/or pore size, particle coordination and fundamental parameters such as diffusion coefficients for different matter transport pathways. However constitutive parameters obtained in these models are rather approximate as they are obtained from analytical solutions for highly simplified grain and pore structures (mostly spherical or cylindrical) [7]. More recently the discrete element method (DEM) has been developed to take multiple particle-particle interactions into account. This approach has been used particularly in modelling constrained sintering [10-15]. It uses the analytical model for sintering of a pair of spherical particles to calculate the forces acting on any given pair in the assembly of particles and then computes their consequent rigid motion [16]. A key feature of the DEM method is that it models the response of typically tens of thousands of particles and is therefore well-suited to simulating semi-macroscopic behaviour. It has been successfully applied to simulate the development of anisotropic microstructure during sinter forging [14], shape distortion and delamination during constrained sintering of ceramic strips [17] and defect evolution (e.g. cracks) in sintering [12]. However, the DEM method requires that the particles are initially spherical and that densification can be simulated by the interpenetration of the initial spheres and described quantitatively by the two-sphere sintering model. Consequently, the initial spherical solid portions that have not overlapped during densification are retained in the evolving microstructure. Hence the approach is suitable for simulating only the early and intermediate stages of sintering. Particle coarsening and shape changes of solid surfaces and

pores, which are extremely important in understanding the detailed microstructure development, and sintering in the later stages, are not included.

The phase field method is capable of modelling real complicated microstructural changes for a wide variety of material processes [18-20]. However a realistic phase field model of sintering including densification is yet to be developed. The obstacle hindering the phase field approach to sintering is associated with the difficulty in treating the particle rigid body motions in an effective way consistent with phase field formalism [20, 21].

Cellular automata (CA) [22-24] and Monte-Carlo (MC) [7, 25-32] methods can be used to model evolution of any complicated microstructure without prohibitive computation cost. In these methods space is discretised into cells (or voxels in 3 dimension). The state of any given cell is allowed to change with advancing time (e.g. from one grain orientation to that of a neighbouring grain if simulating grain growth) determined by simple switching rules. This mimics what happens in reality on an atomistic level and therefore reflects the fundamental energy driving forces and kinetic mechanisms underpinning the microstructure changes. One major advantage of this approach is that both CA and MC have the capability of modelling multiple processes acting simultaneously. For example curvature-driven grain growth and coarsening by surface transport acting in parallel can be taken into account in a CA and MC model [30, 32, 33].

Previously we have used the CA approach in simulating the evolution of the 2D microstructure of materials [23] and the 3D microstructure degradation of nickel/zirconia cermet fuel cell electrodes [22] by evaporation-condensation and grain growth. The CA models have also been shown to reproduce well known phenomena such as wetting, grooving and particle coarsening. Quantitative relationships have been established in those studies between modelling parameters and wetting angle and grain boundary groove angle [23].

However, the potential benefits of CA and MC methods have not yet been fully explored or exploited in sintering. In particular, the process of grain boundary diffusion and resulting grain boundary collapse that leads to densification has not been implemented in the CA-MC approach. This, and calibration of the model parameters in terms of real physical quantities, are necessary to simulate microstructure evolution during sintering of particle assemblies.

In this paper, we first extend our CA-MC simulation approach to matter transport in a sintering body by surface diffusion. We then develop a physically realistic CA-MC methodology to deal with grain boundary diffusion and collapse (which is responsible for densification) that takes

into account the effect of shrinkage mismatch, among different neck-connected particle pairs, on the rigid body motion of particles using the variational principle. To the best of our knowledge, this is the first time that a sintering model can not only account for multiple mass transport mechanisms and deal with real microstructure without simplification, but also treat grain boundary collapse appropriately. The simulations of individual processes (corresponding to different mass transport mechanisms) are calibrated against classical continuum theories using the well-studied two-sphere case. This allows us to establish the quantitative relationship between the CA-MC model parameters and fundamental physical parameters such as surface and grain boundary diffusion coefficients. Finally, we illustrate the use of the methodology by applying it to the sintering of a randomly packed assembly of spherical particles.

2 Methodology

Glossary of symbols

A_{gb} grain boundary area

b grain boundary width.

C normalising parameter describing the interaction energy between two filled cells

C_{mis}^{ij} mismatch coefficient between the cell c_{ij} and the target cell c_x.

D_{ij} inter-particle distance between particle i and j

δD_{ij}, change in inter-particle distance

D_{g} grain size

D_s surface diffusivity

D_B grain boundary diffusion coefficient

E_a activation energy

G total free energy

K time constant for grain growth

L_{ij} circumference length of the grain boundary between particle i and j

n the number (index) of a given time step in the simulation

N_{mv} number of matter voxel moving out of a given grain boundary area in a given time step

N_{tp} total number of triple point (TP) vacant voxels around a given neck between two particles.

N_i^{CO} the number of particles which are in contact with particle i

p_{th} threshold probability for state switch of a triple point voxel, fixed to be 0.1 in this paper

p probability of state switch

P_c capillary pressure

ra random number generated by computer

r_{gb} equivalent radius of a given grain boundary

r_c radius of curvature

T absolute temperature.

Δt_{gb} real time length for each time step in the simulation for GB diffusion and collapse

Δt_{sd} real time length for each time step in the simulation for surface diffusion

U^f energy "imbalance" of a cell sitting on a flat interface

U^x energy imbalance of an interface cell under consideration

Δu^i relative energy (with respective to a flat interface) of cell i

Δu^{ij} energy difference between cell *i* and *j*

Δu^{tp} relative energy of a vacant cell at a triple point

Δu_{ed}^{ref} reference energy set for evaporation and deposition, fixed to be 1.0 in this paper

Δu_{th} the limit set for the state switch for triple point vacant voxel

V_i volume of particle *i*

V_{ij} interaction volume between particle *i* and *j*

x, radius of a circular neck

a radius of spherical particle

γ_{gb} specific grain boundary energy

γ specific surface energy

δ_{ij} Kronecker delta

$\dot{\varepsilon}_{ij}$ inter-particle strain rate between particle *i* and *j*

$\dot{\varepsilon}_M$ macroscopic strain rate

k Boltzmann constant

μ_{ij} inter-particle viscous modulus between particle *i* and *j*

Π sum of free energy change rate and energy dissipation rate

σ_{ij}^{mis} local mismatch stress in the space particle *i* and *j* with respective to matrix

ψ dihedral angle

ψ_{ij}^{diss} dissipation energy

Ω atomic volume

2.1 Energy functions and state switching

In both CA and MC, space is discretised as cells. Each cell is assigned an internal state describing its nature (e.g. solid, pore, surface, interface, crystal orientation) and its internal energy with respect to a common reference energy. The system evolves by the exploring switching the state of the cells according to an energy-based criterion or set of rules. The energy of a given cell depends on its interaction with neighbouring cells which we term "structural imbalance" [22, 23]. In CA, all the cells that are in a position to make a switch to a lower energy state are allowed to switch their state simultaneously (within one time-step). This is applicable to some physical processes (such as evaporation-condensation and grain boundary migration) where the probability of a cell's state switch can be assumed to be independent of the outcome of its neighbour's state switch. When simultaneous state switching cannot be applied (e.g. for grain boundary diffusion and collapse, or surface diffusion) the MC approach is used to decide whether a state switch occurs. When MC is used, one relevant cell is chosen randomly for a decision regarding a state switch. Therefore, time in the MC model is measured in units of a "Monte Carlo step" (MCS) which corresponds to N attempted changes (or sub-steps), where N is the total number of relevant cells.

During sintering, the driving force for matter transport is the free energy change associated with surface curvature. In the classical continuum theories (e.g. Gibbs-Thomson equation) the excess free energy is related to curvature as $\Delta G \propto 1/r_c$ (where r_c is the local radius of curvature). Curvature is a macroscopic concept which is simple, accurate and elegant in dealing with surface/interface energy problems. While the classic Gibbs-Thomson equation is convenient to apply in 2 dimensions or to a sphere, for 3-D non-spherical surfaces a generalized Gibbs-Thomson equation [34] may be used with the two principal curvatures in orthogonal directions $1/r_c = 1/r_1 + 1/r_2$. Johnson's generalized Gibbs-Thomson equation [34] is simple in form but not computationally efficient to apply. Furthermore, the concept of curvature only applies to smooth surfaces and cannot deal with sharp features or edges. Therefore, in order to develop a generally applicable method for computer simulation, it is necessary to use a concept which is not only physically equivalent to curvature for smooth surfaces, but is also computationally more efficient. In our earlier papers we have demonstrated that the concept of "structural imbalance" accurately represents the local energy increase due to the presence of non-balanced bonding at a surface or interface [22, 23] (i.e. bonding that is different from that in the homogeneous bulk material). The quantified structural imbalance of surface and interface

voxels is consistent with the local 'curvature' (the concept used in classical continuum theories) in describing the local energy increase. By using this concept of structural imbalance, interface wetting, grain boundary grooving and grain growth can all be reproduced accurately using cellular automata approach [22, 23]. The concept of energy change due to curvature is thus one way of describing structural imbalance for a smooth surface. Furthermore, the concept of structure imbalance is more generally applicable in dealing with interface energy problems. It can easily accommodate anisotropic surface/interface energies and complicated geometrical features into quantification.

In our modelling approach, all the state switch rules are based on Boltzmann statistics for overcoming an energy barrier of magnitude E_a per atom with respect to a suitable reference state (e.g. a bulk atom). The probability of the reference state atom overcoming the activation barrier is then proportional to $\exp(-E_a/kT)$. If the initial state has, as a result of its position (e.g. it is a surface atom), an energy Δu higher than the reference, then the barrier height is reduced to $E_a-\Delta u$ and the jump probability becomes proportional to $\exp(-E_a/kT)\times\exp(\Delta u/kT)$. Thus the relative probability of a successful jump is exponentially related to its excess energy i.e., $p \propto \exp(\Delta u/kT)$. Since the excess energies tend to be rather small ($\Delta u << kT$), the probability of a successful jump is directly proportional to the excess energy. Applying this to a voxel then gives the result that the probability of a successful state switch of the voxel will be proportional to its excess energy and hence a methodology is required to calculate a parameter proportional to the excess energy of interface and surface voxels.

The relative excess energy of an interface cell due to local curvature can be calculated as [22, 23]

$$\Delta u^x = (U^x - U^f)\,/U^f \qquad \text{Eq. 1}$$

In this equation U^f is the energy "imbalance" of a cell sitting on a flat interface and U^x is that of an interface cell under consideration. The "imbalance" is proportional to the energy of a surface or interface voxel compared with a voxel in the bulk and can be expressed as

$$U^f = c\sum_{i=1}^{n}\left[\frac{(2i+1)^3-(2i-1)^3-8i}{2i(2i-1)^3}\right] \qquad \text{Eq. 2}$$

and

$$\boldsymbol{U^x = C\sum_{i=1}^{n}\frac{\sum_{j=1}^{24i^2+2} C_{mis}^{ij}(1-\delta_{C_x C_{ij}})}{i(2i-1)^3}} \qquad \text{Eq. 3}$$

C is a normalising parameter describing the interaction energy between any two neighbouring solid cells under consideration. Since only relative energy is relevant, C will be cancelled out in Eq.1. i is the number index of the layer in which the neighbouring cell is located. The nearest neighbours are layer 1, the next nearest neighbours are in layer 2, and so on. n is the mask size or the total number of layers to be considered. In 3-D the interaction with voxels in layers beyond layer 2 can be regarded as negligible due to screening effects in the underlying physical processes, so n can be set equal to 2 to save computation time. $\delta_{c_x c_{ij}}$ is the Kronecker delta and C_{mis}^{ij} is the "mismatch coefficient" between a cell in the mask and the target cell. For example, the mismatch coefficient between a cell in a condensed phase and a void cell is taken as 1, whereas that between different condensed phases or crystallite orientations is between 0 and 1.

A consequence of the above formalism is that in the simulations that are described later, the energy parameter appearing in the simulations is dimensionless. This also applies to other parameters such as length, which is measured in units of voxel size, and time which is measured in units of time steps. In order to convert to real world units it is necessary to calibrate the simulation as described later.

2.2 Surface diffusion

Surface diffusion is simulated by considering movement of matter from a surface cell to a neighbouring vacant surface cell in each time step of the simulation. This is done by considering the "detachment" and "attachment" of either vacant voxels or matter (filled) voxels at a surface depending on which is the more efficient for computation in a given situation. (There exists a spectrum of surface transport mechanisms depending on the range of the atomic jumps over the surface. This variety can be reflected in the simulation by changing the range of the possible switching cells.) The rules for redistribution of both vacant and matter voxels are very similar. The following is a description for vacant voxel movement. The process is considered to take place in two consecutive steps: detachment of voxels and their re-attachment elsewhere on the surface. At a detachment step, each surface vacant voxel (i.e. a vacant voxel with a nearest neighbour matter voxel) is allowed a chance of switching its state (i.e., becoming a matter voxel) with a probability proportional to its energy level as expressed by Eq.4.

$$\boldsymbol{p} = \begin{cases} \mathbf{0} & \Delta \boldsymbol{u^i} < \mathbf{0} \\ \frac{\Delta \boldsymbol{u^i}}{\Delta \boldsymbol{u_{ed}^{ref}}} & \Delta \boldsymbol{u^i} > \mathbf{0} \end{cases} \quad \text{Eq. 4}$$

Here Δu_{ed}^{ref} is a reference energy set for detachment and attachment. It is fixed to be 1.0 in this paper. This ensures that Δu_{ed}^{ref} is larger than the highest possible energy of any surface vacant voxel in the system. A non-Metropolis Monte Carlo algorithm [35] is used to make a final decision on whether the detachment of a particular surface vacant voxel is successful or not. A random number *ra* ($0<ra<1$) is generated by the computer and if $ra \leq p$, the state switch is accepted, but if $ra > p$ the switch is rejected. In order to conserve matter, the attachment step requires exploration of a sufficiently large number of attachment attempts so that the number of successful attachments is equal to the number of successful detachments. This is achieved in the following way. In an attachment step, each detached vacant voxel will try to find a matter surface voxel in the neighbourhood to make vacant. Therefore, the attachment step will consist of multiple MC sub-steps with the number of successful sub-steps equal to the number of vacant voxels which successfully switched in the detachment step (which is equal to $\sum_{i \in SV} \frac{\Delta u^i}{\Delta u_{ed}^{ref}}$, with SV being the set containing all the surface vacant voxels having $\Delta u^i > 0$). In each attachment MC sub-step, a detached vacant voxel is randomly selected. Then the matter surface voxel in its Von Neumann neighbourhood (the 6-voxel octahedral neighbourhood) which has the highest energy level is located. This matter surface voxel is allowed a chance of being filled with a vacant voxel with a probability proportional to its energy level as expressed by Eq.4. Again a non-Metropolis Monte Carlo algorithm is used to make a final decision on whether the attachment is successful. If the attachment is not allowed by the Monte Carlo algorithm, the detached vacant voxel goes back to its original position. The detachment step is a typical CA step (which allows all the surface matter voxels to act simultaneously) while the attachment step consists of multiple MC sub-steps. Therefore the surface diffusion model is a CA-MC hybrid model.

The free energy for each matter surface voxel Δu^i (in Eq.4) is calculated using Eq.1-3, with the mismatch constant $C_{\text{mis}} = 1$ for interaction between a surface matter voxel and any vacant voxels in the neighbourhood. For a surface matter voxel next to a triple point boundary (which is not only a surface matter voxel, but also a grain boundary voxel), interaction also exists between matter voxels in different grains, for which C_{mis} has a value between 0 and 1 ($C_{\text{mis}}=\cos(\psi/2)$, with ψ being the equilibrium dihedral angle between the two grains [22]).

Similarly for calculation of the free energy of a vacant surface voxel, C_{mis} also takes the value 1 for interaction between a surface vacant voxel and matter voxels in the neighbourhood. However, a surface voxel next to a triple point boundary will have interactions with matter voxels belong to different grains. In this case, C_{mis} takes the value 1 for the interaction between a surface vacant voxel and a matter voxel belong to the 'home' grain and $C_{mis}=1-\cos(\psi/2)$ for its interaction with a matter voxel belonging to a neighbour grain.

When a matter voxel has been transported to a location on a different grain, the state (i.e. the crystalline orientation) of this matter voxel has to be changed to that of its new 'home' grain Therefore a so-called 'assimilation process' is included in each detachment step of vacant voxels in which all the newly deposited voxels will have to change their crystalline orientation state to those of their new home grains.

2.3 Grain boundary diffusion and collapse (GBDC)

Grain boundary collapse is the mechanism responsible for the shrinkage and densification of the sintering powder body. This requires removal of material from a grain boundary and its transport to an adjoining pore surface and the centres of the adjoining grains moving closer together by a rigid body displacement. According to classical continuum theories the driving force for this is the curvature of the adjoining pores. In our approach, we simulate this same process by energy-based rules controlling the behaviour of grain boundary and surface voxels. It is convenient to represent this process from the point of view of vacant voxels, which is similar to the movement of lattice vacancies in a real material in which vacancies are injected into a grain boundary intersecting a pore and are subsequently annihilated in the boundary by the climb of grain boundary dislocations. The driving force in the simulation is the excess free energy of the vacant voxels at the triple point where a pore and two particles or grains meet (abbreviated as a TP vacant voxel hereafter).

In discretized space, each TP vacant voxel has at least one filled voxel for each neighbouring grain in its Von Neumann neighbourhood. Eqs.1-3 are again used for the calculation of the excess energy of the TP vacant voxels (Δu^{tp}) with $C_{mis} = 1$ for the interaction between a TP vacant voxel and a filled voxel belonging to its 'home' grain and $C_{mis} = 1-\cos(\psi/2)$ for its interaction with a filled voxel belonging to a neighbouring grain. . The probability of a TP vacant voxel to be filled with a matter voxel is proportional to its Δu^{tp} , because Δu^{tp} represents the driving force (curvature). Meanwhile the average migration distance from a matter source to the matter sink (TP) can be assumed to be equal to the equivalent radius of the grain boundary

area. Therefore, in order to determine the state switch probability of a TP vacant cell, the energy term Δu^{tp} needs to be modified, by dividing it by the equivalent radius of the grain boundary. The equivalent radius of grain boundary can be expressed as

$$r_{gb}=(A_{gb}/\pi)^{0.5} \quad \text{Eq. 5}$$

with A_{gb} being the grain boundary area. Thus the state switch probability of a TP voxel will be proportional to:

$$p_{tp}= \pi^{0.5}\Delta u^{tp} /A_{gb}^{0.5} \quad \text{Eq. 6}$$

At each time step, each TP vacant voxel is allowed a chance to be filled with a matter voxel (or in other words, allowed a chance to diffuse into the grain boundary and the grain boundary to subsequently collapse), with a probability described by Eq.6 (a non-Metropolis Monte Carlo algorithm is used to make a final decision on whether it is successful) normalised by a factor p_{th}. The higher p_{th} is set, the smaller is the probability, which corresponds to a smaller time step length. Ideally p_{th} should be set at a value just above the maximum possible value of p_{tp} in the system. For the examples given in this paper a value of 0.1 was found to be appropriate.

To model the grain boundary collapse, at each time step the distance between the centres of adjoining particles or grains (particle i and particle j) changes by δD_{ij}, which is defined as a negative quantity for shrinkage. Therefore, the inter-particle distance at the start of the next time step is $D_{ij}(n+1) = D_{ij}(n) + \delta D_{ij}(n)$. The magnitude of the grain boundary collapse thickness $|\delta D_{ij}|$ depends on the number of newly filled TP voxels at the neck between the two particles (or the number of GB matter voxels which have diffused out of GB area), N_{mv}, and the grain boundary area, A_{gb}, i.e. $\delta D_{ij}=-N_{mv}/A_{gb}$.

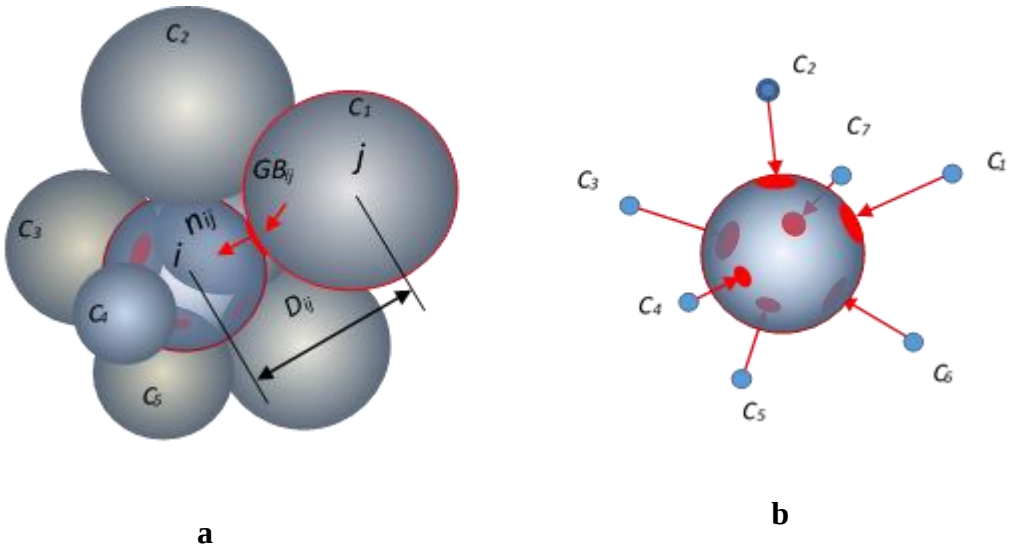

a **b**

Fig.1 a) Schematic of multiple particle interactions: particle *i* with 7 neighbour particles in contact b) Spatial distribution of contacts on particle *i*.

This assumes a uniform collapse of the grain boundary as all the newly vacant voxels in the boundary are annihilated simultaneously. The way in which this is related to shrinkage of the particle assembly is described later. This uniform collapse approach is different from the 'columnar collapse method' adopted by Tikare et al. [30, 36] in their KMC models for sintering. In their method a straight line is projected from the vacant grain boundary voxel through the centre of mass of the adjacent grain to the outside boundary of that particle, and then the vacant grain boundary voxel is exchanged with the filled surface voxel [7, 27, 36]. However, 'columnar collapse' is not as physically realistic as a uniform collapse. It cannot take local mismatch stress into consideration (as described later) and therefore will have difficulty in dealing with rigid body motion.

We now relate the collapse of individual boundaries to the shrinkage of the particle assembly. For modelling the multi-particle situations that are relevant to powder compacts, the individual grain boundaries contacting a given particle or grain will have different collapse distances. Therefore there will be a mismatch in strain, arising from collapse, amongst different neck-connected pairs that has to be considered. As illustrated in Fig1a, particle *i* has 7 neighbouring particles. These necks (grain boundaries) are orientated in different directions as shown in Fig. 1b. In an ideal case of uniformly sized spherical initial particles and uniform grain boundary

size, in a regular packing geometry there would be no mismatch of local strain among different pairs. In such a case the macroscopic shrinkage strain will be the same as the local shrinkage strain arising from local grain boundary collapse. In a real case, the collapse of each individual boundary is constrained by its surroundings (which are different for every grain) to be compatible with each other and with the macroscopic strain. This constraint is manifest as local stresses that either accelerate or oppose the local grain boundary collapse to maintain overall strain compatibility. For free sintering of a powder compact considered here, the macroscopic strain rate may be assumed to be homogenous and isotropic. (This would be modified in the presence of an external constraint, as in sintering a film on a substrate, or a non-isotropic initial packing, as for a die-pressed compact. Such macroscopic constraints can also be accommodated within the general formalism described here.)

We now consider how the local stresses achieve strain compatibility by viscous deformations which are additional to the grain boundary collapse. In principle there is also an elastic contribution to the total strain and an elastic strain rate if the stresses change. However, sintering is carried out under conditions in which viscous strains are much larger than elastic strains and therefore the elastic contribution can be neglected. Consider a pair of particles i and j with an unconstrained grain boundary strain rate of $\dot{\varepsilon}_{ij}$ (negative for collapse leading to shrinkage) = $\delta D_{ij}/D_{ij}$, embedded in the surrounding matrix of particles which has a strain rate of $\dot{\varepsilon}_M$ equal to the macroscopic strain rate (also negative for densification). We define the local effective viscous modulus μ_{ij}, which depends on the local porosity. $\dot{\varepsilon}_{ij}$, $\dot{\varepsilon}_{M,}$ and μ_{ij} are all regarded as constants within a given time step. The difference between the unconstrained grain boundary strain rate and the macroscopic strain rate, $\dot{\varepsilon}_{ij} - \dot{\varepsilon}_M$, can be regarded as the mismatch strain for the pair of particles If a given pair of particle tries to shrink by a strain larger in magnitude than the macroscopic shrinkage strain then a local tensile stress develops to oppose the local unconstrained shrinkage.

In the simulation the unit of time is the time step. Therefore, the increment of strain and the strain rate for a given time step become equal. Thus, $\dot{\varepsilon}_{ij}(n) = \varepsilon_{ij}(n)$ and $\dot{\varepsilon}_M(n) = \varepsilon_M(n)$, with $\varepsilon_{ij}(n)$and $\varepsilon_M(n)$ being the local strain and macroscopic strain generated in time step n. Consequently, the mismatch stress between the bonded pair and the matrix can be written as

$$\sigma_{\mathrm{ij}}^{\mathrm{mis}} = -\mu_{\mathrm{ij}}(\dot{\varepsilon_{\mathrm{ij}}} - \dot{\varepsilon_{\mathrm{M}}}) \qquad \text{Eq. 7}$$

and the energy dissipation associated with local viscous creep during the time step is:

$$\psi_{ij}^{diss} = \mu_{ij}\left(\dot{\varepsilon}_{ij} - \dot{\varepsilon}_M\right)^2 \qquad \text{Eq. 8}$$

The variational principle requires the sum of the rate of change of stored energy and dissipated energy $\Pi = \dot{G} + \Psi$, to be a minimum with respect to the independent variables [37-40].

The independent variable in consideration is the macroscopic strain, so the variational principle can be applied here as:

$$\frac{\partial \psi}{\partial \dot{\varepsilon}_M} + \frac{\partial \dot{G}}{\partial \dot{\varepsilon}_M} = 0 \qquad \text{Eq. 9}$$

The free energy *G* generally can be regarded as the sum of total surface energy, total grain boundary energy and total stored elastic energy. As pointed out earlier, the elastic stored energy change as a function of time is expected to be much smaller than the sum of surface energy and grain boundary energy changes, so it is neglected in this work. In the simulations the surface energy and grain boundary energy minimisations have been dealt with by the AC-MC implementation, and are independent of the macroscopic strain rate. Therefore Eq. 9 can be re-written as:

$$\frac{\partial \psi_{tot}(n)}{\partial \varepsilon_M(n)} = 0 \qquad \text{Eq. 10}$$

The total dissipation energy can be expressed as:

$$\psi_{tot}(n) = 1/2 \sum_{i=1}^{N} \sum_{j \in SC} (\varepsilon_{ij}(n))^2 \mu_{ij}(n) V_{ij}(n) \quad \text{Eq. 11}$$

The factor of ½ in these expressions accounts for the fact that there are two particles in each pair, and the set SC means all the particles which are in contact with particle *i*. The local interaction volume between particles *i* and *j* can be approximated as:

$$V_{ij}(n) = \frac{V_i(n)}{N_i^{CO}(n)} + \frac{V_j(n)}{N_j^{CO}(n)} \qquad \text{Eq. 12}$$

where $V_i(n)$ and $V_j(n)$ are the volumes of the particle *i* and *j* at time step *n*, and $N_i^{CO}(n)$ and $N_j^{CO}(n)$ are the coordination numbers (i.e., the number of particles which are in contact with particles *i* and *j*, respectively) at time step *n*.

Combining Eqs.10-11 leads to:

$$\varepsilon_M(n) = \frac{\sum_{i=1}^{N} \sum_{j \in sc} \mu_{ij}(n) \varepsilon_{ij}(n) V_{ij}(n)}{\sum_{i=1}^{N} \sum_{j \in sc} \mu_{ij}(n) V_{ij}(n)} \qquad \text{Eq. 13}$$

The local viscous modulus is approximated by (assuming a Coble creep mechanism, see the Appendix)

$$\mu_{ij}(n) = {A_{\mathrm{gb}}}^{1.5} D_{ij}(\mathrm{n}) p_{\mathrm{th}} / (L_{ij}(n) \pi^{0.5}) \qquad \text{Eq. 14}$$

where A_{gb} is the grain boundary area, L_{ij} is the circumference length of the neck, and D_{ij} is the distance between the centres of the two particles and p_{th} is the probability normalising factor for the state switch of a triple point voxel.

The local mismatch stress at time step n is calculated by Eq.7. The driving force for sintering at time step n is influenced by the mismatch stress from the previous time step (n–1). This can be taken into account by modifying the excess energy of a grain boundary voxel to give

$$p_{tp}(n) = \pi^{0.5} [\Delta u^{tp} + \sigma_{ij}^{mis}(n-1)] / A_{gb}^{0.5} \qquad \text{Eq. 15}$$

In the simulation, the viscous modulus μ_{ij} is dimensionless and hence the stress σ_{ij}^{mis} is also dimensionless and so can be added to the dimensionless excess energy of a triple point voxel Δu^{tp}.

In summary, simulating grain boundary diffusion and collapse and the resulting shrinkage involves the following procedure in each time step:

1) Calculate the excess energy (Δu^{tp}) for each triple point voxel;
2) Calculate the local driving force using Eq.7 which includes also the influence of local stress from the previous time step;
3) Implement the MC steps for grain boundary diffusion and collapse;
4) Calculate the local strain and the macroscopic strain using the variational principle;
5) Calculate the new local stress which will be used as an input for calculating the driving force for the next time step.

Regarding the morphological change resulting from grain boundary collapse, for the two-sphere case it is treated as happening when the accumulated change in boundary thickness is equal to, or larger than, one layer of voxels (i.e., $\Sigma(\delta Dij(n) A_{\mathrm{gb}}(n) \geq A_{\mathrm{gb}}(n))$. At that point one whole layer of grain boundary cells will be removed. This way of dealing with grain boundary collapse is disruptive, but it is implementable in the case of two spherical particles. However, for multi-particle, or powder compact cases, this step-wise disruptive treatment is not appropriate. For the simulation of the free sintering of a powder compact, an isotropic shrinkage can be assumed. Therefore, in order to efficiently deal with the morphology changes arising from grain boundary collapse, the following are also required:

6) After each time step, the voxel size is changed by a factor $1+\varepsilon_M$ so that the whole volume of the sintering body changes by a single factor, and

7) A number of new matter voxels is deposited on particle surfaces to compensate the mass loss due to the decrease of the voxel size, so that mass conservation is maintained. This extra step of deposition is similar to that described in section 2.2 for condensation after evaporation. The resulting modifications to the shapes of the grain surfaces meet the overall requirement of energy minimization in that time step and therefore should be close to reality.

3 Calibration with Classical Theory

In this section known solutions for the sintering of two spheres are used to calibrate the parameters used in the simulations in terms of the macroscopic surface and grain boundary diffusion coefficients. The methodology is illustrated using nickel as an example material. We have considered nickel as a model material because the key energy and mass transport parameters have been measured independently in this case.

The two-sphere model (as shown in Fig.2a) is used for calibration because it is a simple geometry with well-known solutions based on classical continuum theories [2-4, 41-45].

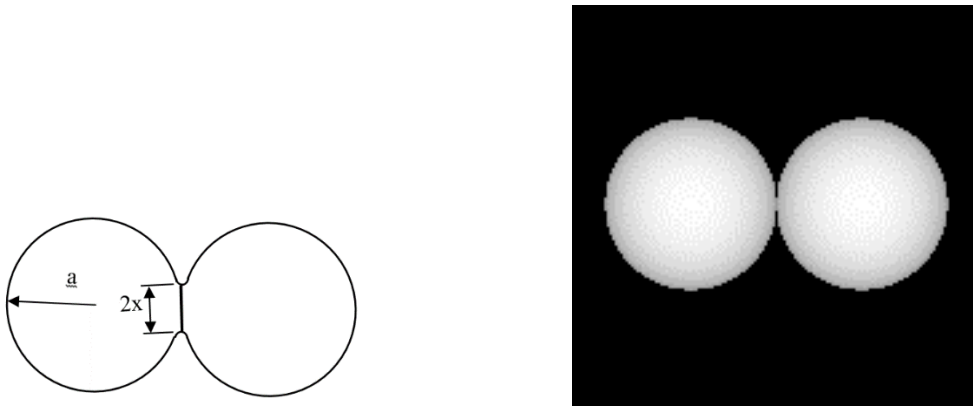

Fig.2 a) The two-sphere model, composed of two identical spherical particles with one growing neck; *a* is the radius of the spherical particles and *x* is the radius of the neck, b) the initial state of the two spheres in CA-MC simulation.

For the CA-MC simulation, each spherical particle (in Fig.2b) was discretised into ~142,000 voxels (all voxels in this work are of cubic shape), with radius a=32.1 (units of distance are voxel size in the simulation). The initial distance between the sphere centres is 32 and the initial neck size is 2.18, as shown in Fig.2b. For the purpose of simplicity each particle is assumed to

be one crystallite and therefore there is only one grain boundary, which is coincident with the neck.

3.1 Surface diffusion

As described in section 2.1, in the CA-MC simulation of surface diffusion, the two variables which affect the kinetics of system evolution are the dihedral angle (through the parameter C_{mis} in Eq.3) and Δu_{ed}^{ref} (in Eq.4). After 500 time steps of surface diffusion in the simulation, the two spheres in Fig.2b have evolved into the configuration shown in Fig.3a. Surface diffusion leads to neck growth, but does not lead to shrinkage. Fig.3b shows how the neck size increases with number of time steps for different dihedral angles. It is clear that the higher the dihedral angle, the faster is the neck growth, which is consistent with the numerical analysis results of Bouvard - McMeeking [41] and Zhang - Schneibel [43] based on classical theory.

There are several analytical expressions available in the literature for describing the kinetics of neck growth by surface diffusion from the continuum theory. These analytical equations have different forms and show different time dependence, which result from different simplifying assumptions, especially regarding the neck curvature. Some of these equations listed in [46] are regarded as incorrect. Nevertheless some of the analytical equations have been shown to be quite reliable and accurate [41]. One such example is the kinetic equation of Coblenz et al. [42]:

$$\frac{x^5}{a} = \frac{225 D_S \gamma \Omega \delta_s}{kT} t \qquad \text{Eq. 16}$$

where γ is the surface free energy, Ω atomic volume, δ_s surface thickness ($\sim\Omega^{1/3}$), D_s surface diffusivity, a radius of the spheres, k Boltzmann constant, and T absolute temperature. Another equation is by Nichols and Mullins [45]

$$\frac{x^6}{a^2} = \frac{25 D_S \gamma \Omega^{1.333}}{kT} t \qquad \text{Eq. 17}$$

Based on their numerical analysis, Bouvard and McMeeking [41] concluded that in the very early stage, the neck growth rate should be lower than that predicted by either of the two equations. Fig.3b clearly shows our simulation points to the same conclusion: before 30 time steps, the simulated neck size is smaller than that predicted by Eqs.16 and 17. After 30 time steps, the simulated neck growth is fairly close to the analytical solutions.

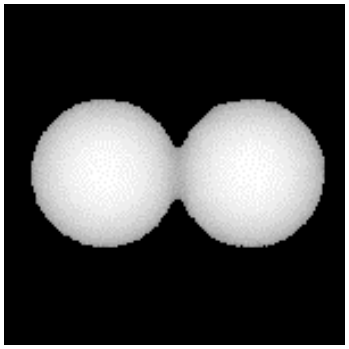

a

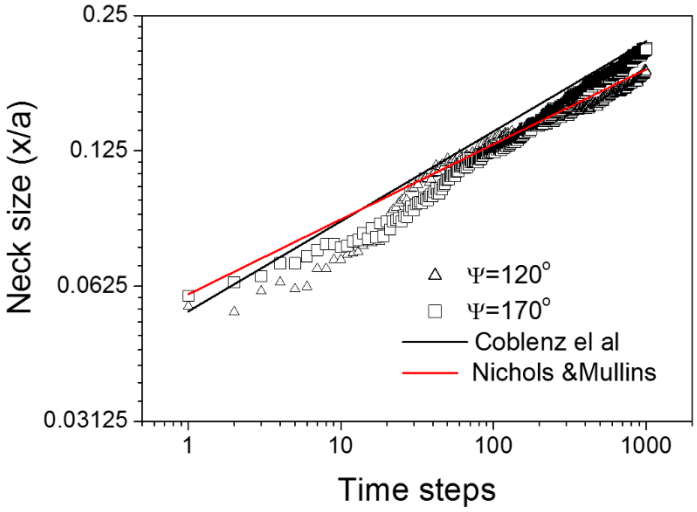

b

Fig.3 a) Neck formation between the two spheres after 500 time steps of simulated surface diffusion (from the initial state shown in Fig.2b); b) simulated neck growth compared with fitting to analytical expressions.

The simple analytical expressions in Eqs.16 and 17 also do not account for the influence of dihedral angle on neck growth which reflects the influence of the grain boundary energy. Nevertheless, they are still useful for describing the relationship between neck growth and diffusivity at longer times. This is seen in Fig3b where the power of time (1/5 or 1/6) predicted by the equations matches the simulations sufficiently well to allow quantitative calibration of the CA-MC parameters. Using the Coblenz equation (Eq.16) the real time length for each simulation time step can be written as:

$$\Delta t_{sd} = \left(\frac{x}{a}\right)^5 \frac{kTa^4}{D_S \Omega \gamma_s \delta_s n_s} \qquad \text{Eq. 18}$$

where n_s is the number of time steps in the simulation and Δt_{sd} is the real time length for each time step in the simulation of surface diffusion. Space discretization has a major influence on Δt_{sd} because the larger the voxel size, the longer the real time corresponding to each time step (according to Eq 18, Δt_{sd} is proportional to the fourth power of voxel size).

3.2 Grain boundary diffusion and collapse (GBDC)

It is well established that GB collapse leads to both neck growth and shrinkage. According to Coblenz [42], the neck growth kinetics by GBDC can be expressed by:

$$\boldsymbol{x^6 = \frac{192\gamma\Omega b D_B a^2}{kT} t} \qquad \text{Eq. 19}$$

Meanwhile the shrinkage can be expressed as:

$$\boldsymbol{\frac{w}{a} = \left(\frac{3\gamma\Omega b D_B}{kTa^4} t\right)^{1/3}} \qquad \text{Eq. 20}$$

The meaning of symbols in Eqs. 19 and 20 is similar to those in Eq.18, with D_B as the GB diffusion coefficient and w in Eq.20 is the decrease of the distance from the centre of one of the spheres to the centre of the grain boundary.

The simulated neck growth results for different dihedral angles caused by GBDC are shown in Fig.4a. The step wise feature in Fig.4a is an artefact as a result of the disruptive treatment of collapse used in the two sphere case. The numerical modelling of Bouvard and McMeeking (Fig.3 in [41]) found that the initial neck growth rate by GBDC should also be slower than that predicted by the Coblenz equation. Our simulation results in Fig.4a show the neck growth in the initial 8 time steps is indeed slower than the Coblenz prediction, which is consistent with the numerical modelling result in [41].

The simulated shrinkage results are given in Fig.4b, which shows a faster shrinkage increase in the initial stage (before 30 time steps), which is again in consistent with the numerical simulation results by Bouvard and McMeeking [41]. However after 30 time steps the shrinkage kinetics matches the Coblenz equation (Eq.20) quite well. From Figs.4a and b it is clear that, with an increase in dihedral angle, the neck size is slightly increased while shrinkage is slightly decreased. This is also qualitatively consistent with the numerical simulation results of Bouvard and McMeeking (Figs.3 and 4 in [41]). To calibrate the GBDC model the simulated shrinkage data were fitted to Eq.20 and the neck growth data to Eq.19. It was confirmed that the GBDC parameters could fit both Eq.19 and Eq.20 simultaneously. For example, if the grain boundary diffusivity is 2.27×10^{-12} m^2 s^{-1} (corresponding to nickel at 923 K) , and when voxel size, threshold probability for state switch and dihedral angle (the three model parameters) are set

to be 100 nm, 0.1 and 120˚ respectively, the real time length Δt_{gb} is found to be 9.95 s when calibrated using simulated neck growth data and Eq.19, and 10.1 s using simulated shrinkage data and Eq.20. From Eqs.19 and 20, Δt_{gb} is proportional to the fourth power of voxel size.

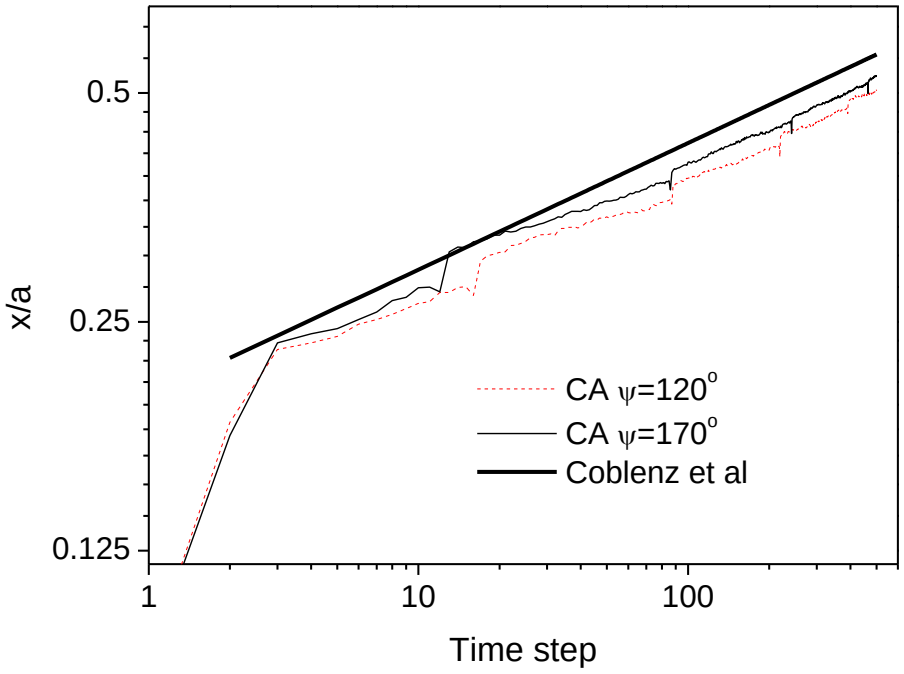

a)

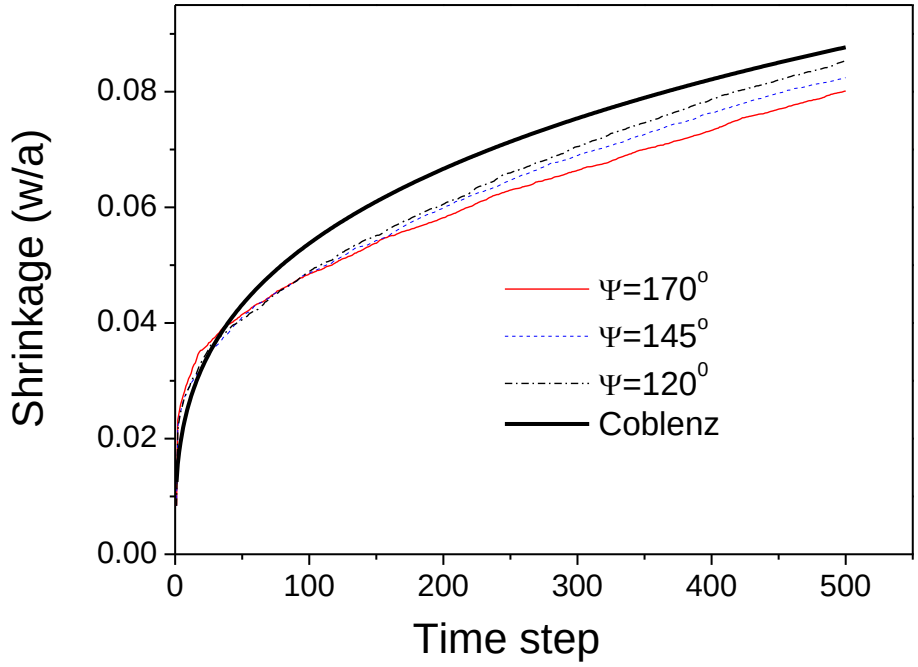

b)

Fig.4 a) Simulated neck growth kinetics b) simulated shrinkage for the case of two contacting spheres sintering by grain boundary diffusion and collapse compared with the predictions of the Coblenz analytical equations. Each simulation step consists of one step of GBDC and one step of surface diffusion as described in section 2.3 and 2.2, respectively.

3.3 Grain Growth

To calibrate the grain growth simulation, a fully dense polycrystalline microstructure was generated with an average crystallite size of 1.1µm and then evolved over 300 time steps. The initial microstructure was generated using the Monte Carlo method within a total volume of 100 × 100 × 100 voxels with a size of 0.2 µm and periodic boundary conditions. The initial microstructure is shown in Fig.5a. The microstructure at time step 300 is given in Fig.5b. The grain growth kinetics simulated is shown in Fig.6.

a) 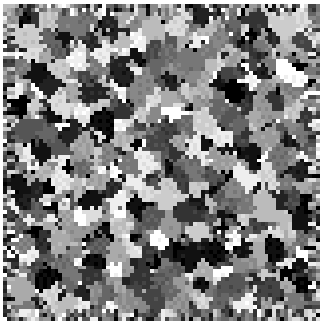 b) 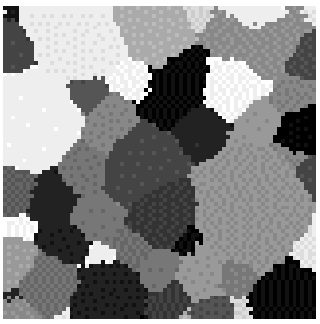

Fig. 5 a) the initial microstructure generated by Monte Carlo method and b) the simulated microstructure at time step 300.

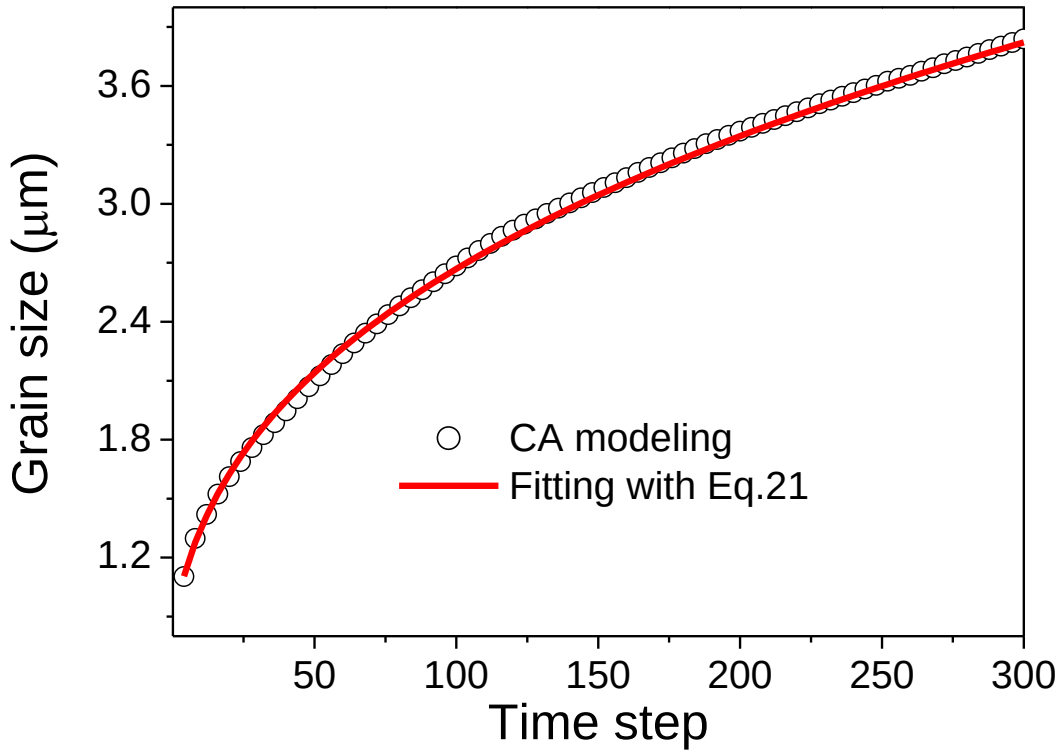

Fig.6 Simulated grain growth and the fitting by $D_g^3 - D_{g,o}^3 = Kt$ for a case in which the reference energy for grain boundary switching increases by 0.16% per time step, whci mimics a boundary mobility decreasing with time due to increasing impurity segregation and "drag",

Grain growth kinetics are often expressed by:

$$\boldsymbol{D_g^m - D_{g,o}^m = Kt} \quad \text{Eq. 21}$$

Where D_g and $D_{g,o}$ are the final grain size and initial grain size respectively, K is a constant, t is the time, and m is the power index. In reality m is found experimentally to vary over a wide range of values. For example, m varies from 2-7 for nanostructured nickel [47, 48], while in the micrometer range (e.g. grain size > 0.3 μm) the kinetics of nickel grain growth appear to fit $m = 3$ well (e.g., the data shown in Fig. 2 of [47]). From the simulation point of view, we found m can vary from 2 to 20 when restrictions (such as boundaries having different mobility depending on misorientation) are put on some of the grain boundaries, or the reference energy difference for state switching changes with the time step. Our earlier work has shown that for the simplest case (in which grain boundary energy is assumed to be isotropic and the reference energy difference for a GB cell state switch is constant), the simulation results (Fig.4e in [23]) fit Eq. 21 well with $m = 2$, which is consistent with the analytical and simulation results of other workers [49, 50]. As an example of departure from $m = 2$, we can simulate the value of 3 observed experimentally for nickel by decreasing the mobility as a function of time. Fig.6 shows the grain growth kinetics for a case where the reference energy difference in the CA model is set to increase at a rate of 0.16% per time step. This mimics a situation in which a 'pinning effect' increases with time (e.g., as a result of impurity enrichment at the grain boundaries [51]). In this case the simulation results fit Eq.21 with $m = 3$.

4 Simulation of sintering an assembly of spherical particles in random packing

Random particle packing was used to specify the initial state of the compact in the simulations as being representative of a typical powder body. In the computer spherical particles were dropped into a container, one by one, from the top of the container. Each particle was allowed to roll without friction to its most stable position between other particles already settled, or between settled particles and container walls.

The particles were assumed to be spherical of the same size of 3 μm. The container size was 20μm × 20μm × 20μm. Our random packing code typically leads to a packing density of 0.61. A representative volume of 15μm × 15μm × 15μm of the particle assembly was chosen for simulation. This volume was taken from the central part of the container volume to avoid the possible influence of the container walls on the packing. The simulation volume contained

about 140 particles. Mirror boundary conditions were applied at the boundaries of the representative volume.

Fig.8 shows the simulated densification, the average pore size and the average grain size as a function of time step, by assuming grain boundary diffusion and collapse as the dominating mechanism. The average pore size was calculated using the linear intercept method [52]. The grain size was taken as the diameter of an equivalent sphere with the same volume. For all the simulations in this paper, an initial voxel size of 100 nm was used. As shown in Fig.8, the average particle size remains almost as a constant. This is because the presence of pores does not allow free grain boundary migration in the early stage of densification.

The microstructure evolution with time step is illustrated in Fig.9. In the initial stage of the random packing (Fig.9a), the packing density is clearly not uniform. It contains both densely packed areas and loosely packed areas. The dense packing regions densify much faster than the rest of the simulated volume. By comparing Fig.9 b and c with a, it is not difficult to see the small pores disappear much faster than the relatively large pores. The region with local low packing density is observed to lead to a large sintering defect, which survives to the very late stage (300^{th} time step). It seems that all the pores, whether small or large, tend to decrease in size, leading to a decreasing average pore size during the whole simulated time as shown in Fig.8.

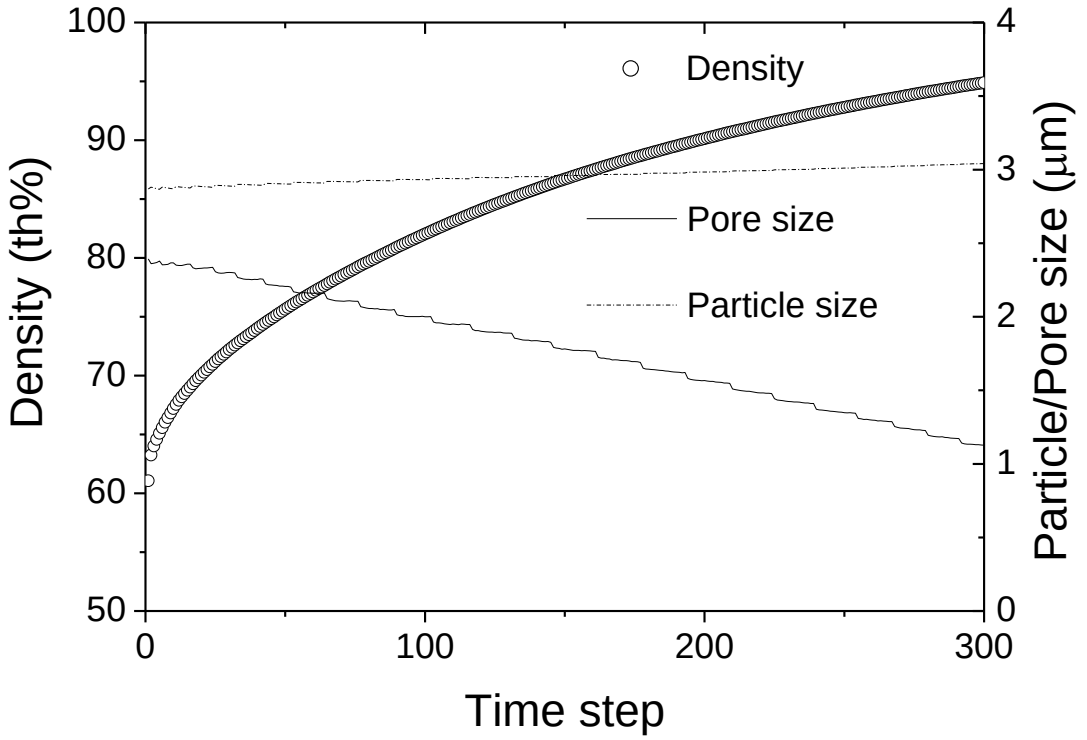

Fig.8 Evolution of microstructure, density, pore size (equivalent diameter) and grain (particle) size (equivalent diameter) as a function of time step obtained by CA-MC simulation.

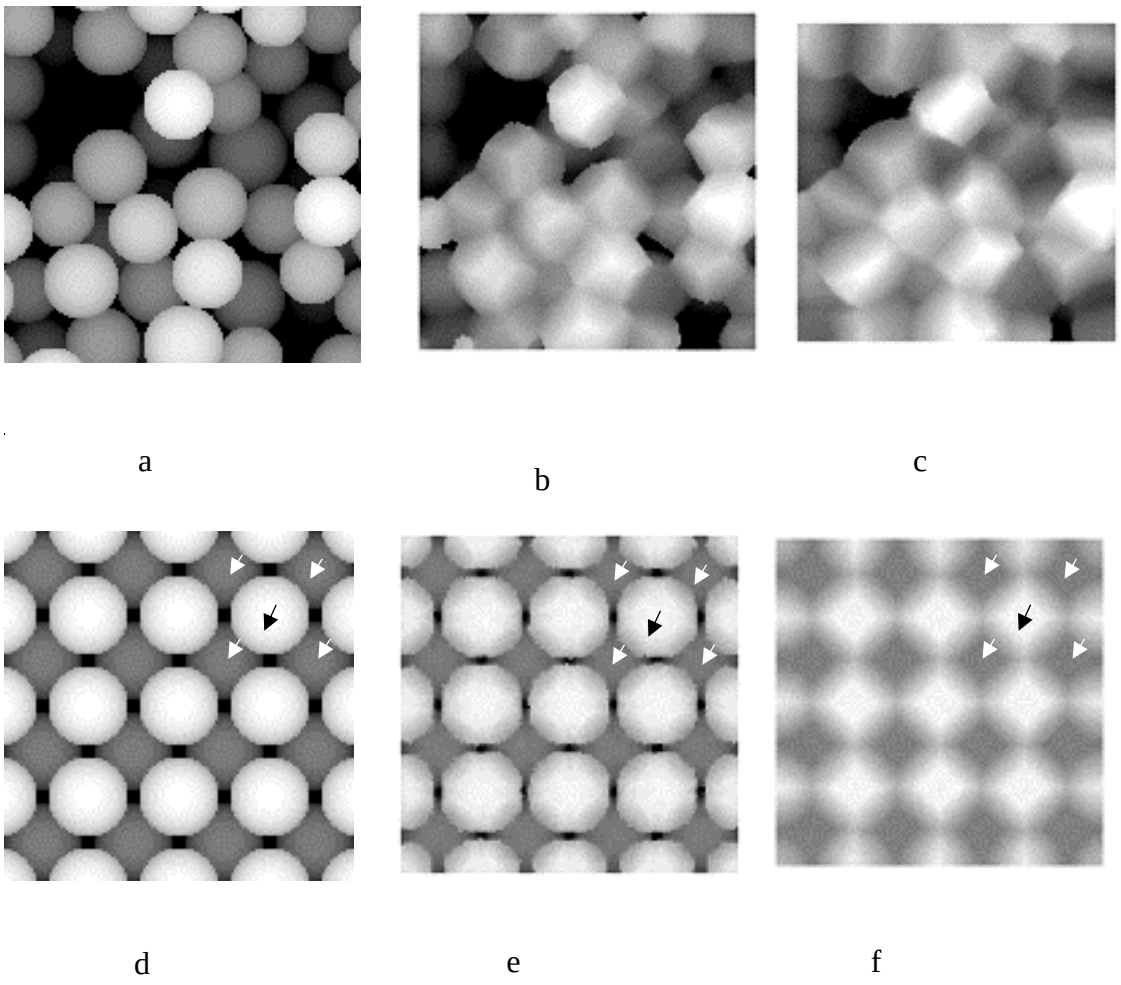

Fig.9 Simulated microstructure at different stages of sintering for a randomly packed assembly of spherical particles: a) initial state; b) after 68 time steps; and c) after 300 time steps. Simulated evolution for a bcc packing of spheres: d) initial state; e) after 12 time steps; and f) after 70 time steps. Note that in d), e) and f) two layers are shown, with the top layer being indicated by dark arrows and second layer by white arrows. Each sphere in the top layer sits on four spheres at second layer.

To provide further insight, Fig.10 shows the simulated shrinkage curve of the randomly packed assembly compared with that for two isolated spheres having the same size (30 μm in diameter) as the randomly packed particles. The linear shrinkage is given directly by the simulation and is used here to compare with the case of two particles for which volumetric densification is not appropriate. It is clear that the random packing leads to much slower shrinkage. This is because the mismatch of local shrinkage (as described in section 3.2) in the random packing case, exerts a restraining influence that is absent in the case of two isolated particles. Figs.9 and 10 also shows the sintering simulations for assemblies of equal sized spheres (also 30 μm in diameter)

in body-centred cubic packing (BCC). This ideal BCC packing has a higher initial density of 0.68 and good uniformity of local curvature and neck size. Therefore there is no mismatch in local densification and no corresponding restraint on densification. As expected, the initial shrinkage of the BCC assembly is the same as that of two spheres (shown in Fig.10), but quickly becomes faster than that of the two sphere case and stops at about the 40^{th} time step as the density approaches 100 %. (The inflection seen in the BCC curve in Fig.10 is an artefact caused by the relatively small number of particles and the boundary conditions used in the simulation). The fast sintering rate is due to the fact that the channels between the neighbouring particles (not in contact initially) gradually become narrower with the time and eventually turn into closed pores. This leads to a higher curvature and higher driving force for sintering. In contrast the neck curvature in the two sphere case always becomes smaller with time. This illustrates the limitations of a simple two sphere model and highlights the importance of having available real 3-D models which not only take care of 3-D microstructure details, but also take into account the local strain rate mismatch caused by packing irregularity.

Fig 10 also shows shrinkage curves for two other ideal packing cases: i.e., face-centred cubic (FCC) packing and simple cubic (SC) packing. Both SC and FCC show a similar shrinkage rate to that of two spheres in the initial stage. Although the initial packing density of SC (0.53) and that of FCC (0.74) are very different from that of BCC (0.68), they all show a similar shrinkage rate in the initial stage, indicating that early stage densification in these ideal periodic geometries is more dependent on the uniformity of the microstructure than the porosity.

When the sintering of these ideal periodic geometries goes beyond the initial stage, the inter-particle channels will evolve into different geometries and therefore the sintering driving force becomes different. For example in the case of FCC, it has the smallest inter-particle channels amongst these ideal periodic geometries. Therefore it has a slightly faster densification at an early stage. In the case of SC, because it has relatively lower density and larger inter-particle channels, it shows a slightly slower densification in the early stage. For example, the density of the SC arrangement has only reached 0.72 at time step 80. At this stage, the inter-particle channels are mostly still open pores and therefore its densification kinetics are similar to the two sphere case.

Both the FCC and BCC arrangements have a high initial density and show significant slowing down as they approach full density. In the case of FCC, densification slows down noticeably at a shrinkage of approximately 0.065 (roughly corresponding to a density of 0.9). In the case of the BCC arrangement, densification slows down noticeably at a shrinkage of 0.105 (or

density of 0.95). The slowing down of densification can be attributed to the microstructure heterogeneity which develops in the late stage of the simulated sintering, namely that some of the pores are eliminated earlier than others. This variability occurs in the simulated microstructures due to the Monte-Carlo approach used in the simulation. The resulting microstructure heterogeneity leads to more local stress mismatch, which hampers the densification.

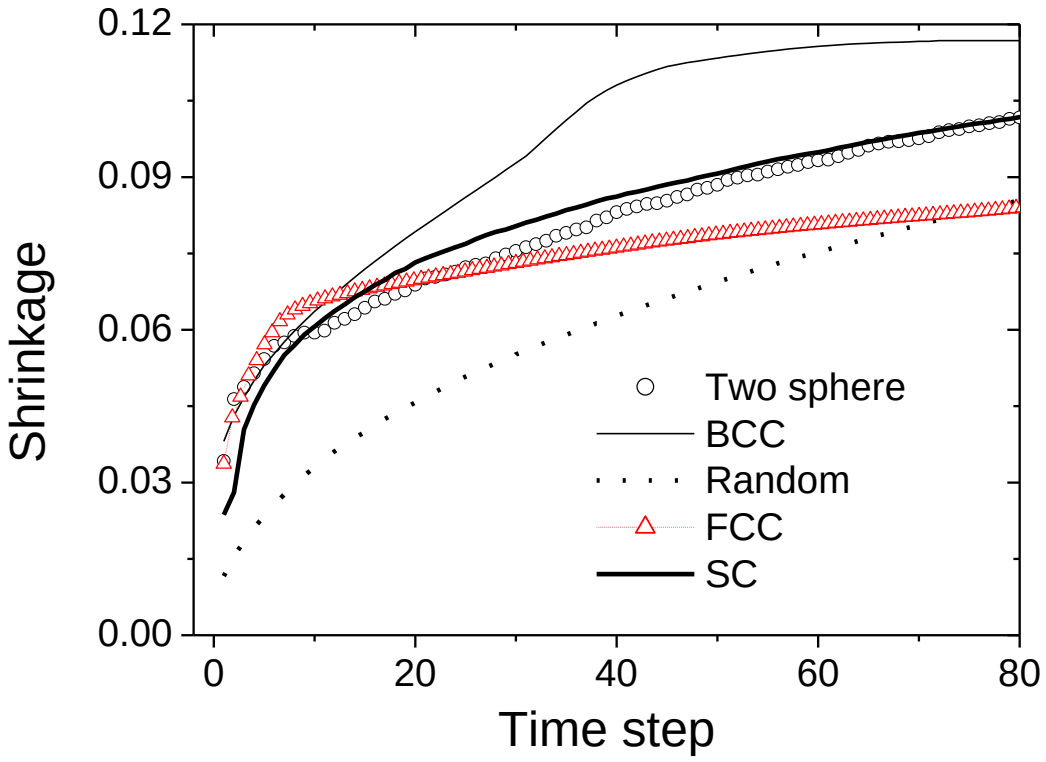

Fig.10 Simulated linear shrinkage kinetics for a randomly packed assembly of spheres, assemblies of spheres in regular packing (BCC, FCC and SC) and two isolated spheres (all spheres have the same size).

5 Summary and Conclusions

A Cellular Automata-Monte Carlo (CA-MC) approach for simulating sintering of particulate materials has been presented, which extends an earlier implementation of this method to include surface diffusion and grain boundary diffusion and collapse leading to densification.

It has been shown that the CA-MC simulation results for the sintering of two identical spherical particles are consistent with those of analytical expressions for the kinetics of neck growth and densification. The quantitative comparison between the simulated kinetics and the analytical expressions allows the simulation parameters to be related to real mass transport parameters (e.g. surface and grain boundary diffusion coefficients, and grain boundary migration rate).

A method for dealing with grain boundary diffusion and collapse has been developed which takes into account the local shrinkage mismatch between pairs of particles in the sintering body. This has shown that shrinkage of a randomly packed assembly of spherical particles is significantly slower that of two isolated particles due to the restraining effects of interaction between particles. In contrast an ideally regular packing of spheres (body centred cubic packing) shows a similar shrinkage rate to that of two isolated spheres in the early stage of sintering because the uniform nature of the arrangement of particles produces no restraining interactions. Thus it has been demonstrated that both microstructure details and local mismatch in interactions between particles are important for accurately simulating sintering.

Appendix

A. Viscosity of two particles bonded by a neck

The viscous modulus is defined as $\mu = \sigma/\dot{\varepsilon}$**,** where σ is the stress and $\dot{\varepsilon}$ is the strain rate. The driving force for sintering by grain boundary diffusion is the difference between the chemical potential of atoms at the neck surface and those at the grain boundary. This chemical potential difference is equivalent to a stress (σ), or capillary pressure (P_c), induced by surface tension around the circumference [2, 53]. Therefore, the driving force for atoms moving from the boundary to the neck is proportional to the capillary pressure which is determined by surface energy. With $\sigma = -P_c$, the local viscous modulus can thereby be expressed as $\mu = -P_c/\dot{\varepsilon}$. According to our previous papers [22, 23], the capillary pressure can be described by the average energy (Δu^{tp}) of the vacant voxels at triple points:

$$P_c=\sum_{i\in \mathbf{TP}} \Delta \boldsymbol{u}^{\mathbf{tp}}(\boldsymbol{i}) \, /N_{tp} \qquad \text{Eq. a 1}$$

where the TP set includes all the TP vacant voxels and N_{tp} is the total number of TP vacant voxels around the neck.

As shown in Fig.1, assuming all the voxels at TPs along the periphery of the neck have the same energy Δu^{tp}, then according to Eq. 9, the probability of a state switch $P = \Delta u^{tp}/[(A_{GB}/\pi)^{0.5} u_{th}]$, with A_{GB} being the grain boundary area. Thus in each time step the number of voxels which would move out of the grain boundary, $N_{mv} = PL_{ij}$, with L_{ij} being the circumference of the neck between particles i and j. The distance between the two central points of the particles would be shortened by $\Delta L=N_{mv}/A_{GB}$. The strain rate is $\dot{\varepsilon} = -\dot{e} = -\Delta L/D_{ij}$ with D_{ij} being the distance between the two central points of the particles. Therefore

$$\mu = \boldsymbol{A_{GB}}^{\mathbf{1.5}} \boldsymbol{D_{ij}} \boldsymbol{p_{th}} / (\boldsymbol{L_{ij}} \boldsymbol{\pi}^{\mathbf{0.5}}) \qquad \text{Eq. a 2}$$

For a pair of spherical particles of an equal radius of a and a neck size of x, $A_{GB}=\pi x^2$, $L_{ij}=2\pi x$ and $D_{ij} = 2a$, Eq.a1 can be simplified as

$$\mu = x^2 a \, \boldsymbol{p_{th}} \qquad \text{Eq. a 3}$$

For a fully dense material, x can be regarded as equal to a, and therefore the viscosity for a fully dense polycrystalline material should be proportional to a^3, which is consistent with Coble's derivation [54] of the viscosity for boundary controlled creep of a polycrystalline material:

$$\mu = f(T, D_B)\, a^3 \qquad \text{Eq. a 4}$$

Correspondingly, in Eq. a2, p_{th} implicitly contains the information regarding temperature and grain boundary diffusion rate.

Acknowledgements

This work was carried out as part of UK EPSRC Grant EP/M014045/1 (Electrodes by Design - Microstructural Engineering of High Performance Electrodes for Solid Oxide Fuel Cells).

References

[1] W.D. Kingery, M. Berg, Study of the Initial Stages of Sintering Solids by Viscous Flow, Evaporation-Condensation, and Self-Diffusion. Journal of Applied Physics 1955;26:1205.

[2] D.L. Johnson, New Method of Obtaining Volume, Grain-Boundary, and Surface Diffusion Coefficients from Sintering Data. Journal of Applied Physics 1969;40:192.

[3] G.C. Kuczynski, Self-diffusion in sintering of metallic particles. AIME TRANS 1949;185:169-178.

[4] R. Coble, Initial sintering of alumina and hematite. Journal of the American Ceramic Society 1958;41:55-62.

[5] G.W. Scherer, Viscous Sintering of a Bimodal Pore‐Size Distribution. Journal of the American Ceramic Society 1984;67:709-715.

[6] T.H. Lim, D. McCarthy, S.C. Hendy, K.J. Stevens, S.A. Brown, R.D. Tilley, Real-time TEM and kinetic Monte Carlo studies of the coalescence of decahedral gold nanoparticles. Real-time TEM and kinetic Monte Carlo studies of the coalescence of decahedral gold nanoparticles 2009;3:3809-3813.

[7] E.A. Olevsky, V. Tikare, T. Garino, Multi-Scale Study of Sintering: A Review. Journal of the American Ceramic Society 2006;89:1914-1922.

[8] J. Svoboda, H. Riedel, Quasi-equilibrium sintering for coupled grain-boundary and surface diffusion. A diffusional creep law for powder compacts 1995;43:499-506.

[9] J. Pan, A. Cocks, J. Rödel, R. Huang, H.N. Ch'ng, Densification of Powder Compact Containing Large and Small Pores. Journal of the American Ceramic Society 2009;92:1414-1418.

[10] C.L. Martin, R.K. Bordia, The effect of a substrate on the sintering of constrained films. Acta Materialia 2009;57:549-558.

[11] B. Henrich, A. Wonisch, T. Kraft, M. Moseler, H. Riedel, Simulations of the influence of rearrangement during sintering. Acta Materialia 2007;55:753-762.

[12] C.L. Martin, H. Camacho-Montes, L. Olmos, D. Bouvard, R.K. Bordia, Evolution of Defects During Sintering: Discrete Element Simulations. Journal of the American Ceramic Society 2009;92:1435-1441.

[13] F. Parhami, R. McMeeking, A network model for initial stage sintering. Mechanics of materials 1998;27:111-124.

[14] A. Wonisch, O. Guillon, T. Kraft, M. Moseler, H. Riedel, J. Rodel, Stress-induced anisotropy of sintering alumina: Discrete element modelling and experiments. Acta Materialia 2007;55:5187-5199.

[15] W. Soppe, G. Janssen, B. Bonekamp, L. Correia, H. Veringa, A computer simulation method for sintering in three-dimensional powder compacts. A computer simulation method for sintering in three-dimensional powder compacts 1994;29:754-761.

[16] C.L. Martin, L.C.R. Schneider, L. Olmos, D. Bouvard, Discrete element modeling of metallic powder sintering. Scripta Materialia 2006;55:425-428.

[17] T. Rasp, C. Jamin, A. Wonisch, T. Kraft, O. Guillon, C.H. Hsueh, Shape Distortion and Delamination During Constrained Sintering of Ceramic Stripes: Discrete Element Simulations and Experiments. Journal of the American Ceramic Society 2012;95:586-592.

[18] L.-Q. Chen, Phase-Field Models for Microstructure Evolution. Annual Review of Materials Research 2002;32:113-140.

[19] Z. Jiao, N. Shikazono, Simulation of Solid Oxide Fuel Cell Anode Microstructure Evolution Using Phase Field Method. Journal of the Electrochemical Society 2013;160:F709-F715.

[20] Y.U. Wang, Computer modeling and simulation of solid-state sintering: A phase field approach. Acta Materialia 2006;54:953-961.

[21] A. Kazaryan, Y. Wang, B.R. Patton, Generalized phase field approach for computer simulation of sintering: incorporation of rigid-body motion. Scripta Materialia 1999;41:487-492.

[22] X. Wang, A. Atkinson, Modeling Microstructure Evolution of Ni Cermet Using a Cellular Automaton Approach. Journal of the Electrochemical Society 2014;161:F605-F614.

[23] X. Wang, Modelling and understanding materials microstructure evolution driven by interface energy. Computational Materials Science 2015;107:1-7.

[24] X. Wang, A. Atkinson, Cellular Automata Modelling of Microstructure Evolution of Ni Cermet Anode. ECS Transactions 2013;57:2465-2473.

[25] G.N. Hassold, I.W. Chen, D.J. Srolovitz, Computer Simulation of Final - Stage Sintering: I, Model Kinetics, and Microstructure. Journal of the American Ceramic Society 1990;73:2857-2864.

[26] K. Mori, H. Matsubara, N. Noguchi, Micro–macro simulation of sintering process by coupling Monte Carlo and finite element methods. Micro–macro simulation of sintering process by coupling Monte Carlo and finite element methods 2004;46:841-854.

[27] V. Tikare, M. Braginsky, E. Olevsky, D.L. Johnson, Numerical Simulation of Anisotropic Shrinkage in a 2D Compact of Elongated Particles. Journal of the American Ceramic Society 2004;88:59-65.

[28] A.G. Sault, V. Tikare, A new Monte Carlo model for supported-catalyst sintering. Journal of Catalysis 2002;211:19-32.

[29] M. Braginsky, V. Tikare, E. Olevsky, Numerical simulation of solid state sintering. Numerical simulation of solid state sintering 2005;42:621-636.

[30] V. Tikare, M. Braginsky, E.A. Olevsky, Numerical Simulation of Solid - State Sintering: I, Sintering of Three Particles. Journal of the American Ceramic Society 2003;86:49-53.

[31] Y. Zhang, C. Xia, M. Ni, Simulation of sintering kinetics and microstructure evolution of composite solid oxide fuel cells electrodes. International Journal of Hydrogen Energy 2012;37:3392-3402.

[32] Z. Yan, Y. Kim, S. Hara, N. Shikazono, Prediction of La0.6Sr0.4Co0.2Fe0.8O3 cathode microstructures during sintering: Kinetic Monte Carlo (KMC) simulations calibrated by artificial neural networks. Journal of Power Sources 2017;346:103-112.

[33] Y. Zhang, M. Ni, M. Yan, F. Chen, Thermal aging stability of infiltrated solid oxide fuel cell electrode microstructures: A three-dimensional kinetic Monte Carlo simulation. Journal of Power Sources 2015;299:578-586.

[34] C.A. Johnson, Generalization of the Gibbs-Thomson equation. Surface Science 1965;3:429-444.

[35] D. Raabe, R.C. Becker, Coupling of a crystal plasticity finite-element model with a probabilistic cellular automaton for simulating primary static recrystallization in aluminium. Modelling and Simulation in Materials Science and Engineering 2000;8:445.

[36] V. Tikare, M.V. Braginsky, D. Bouvard, A. Vagnon. An experimental validation of a 3d kinetic, monte carlo model for microstructural evolution during sintering. Advances in Science and Technology, vol. 45: Trans Tech Publ, 2006. p.522-529.

[37] X. Wang, A. Atkinson, Microstructure evolution in thin zirconia films: Experimental observation and modelling. Acta Materialia 2011;59:2514-2525.

[38] A. Cipitria, I.O. Golosnoy, T.W. Clyne, A sintering model for plasma-sprayed zirconia TBCs. Part I: Free-standing coatings. Acta Materialia 2009;57:980-992.

[39] J. Pan, A. Cocks, S. Kucherenko. Finite element formulation of coupled grain-boundary and surface diffusion with grain-boundary migration. Proceedings of the Royal Society of London A: Mathematical, Physical and Engineering Sciences, vol. 453: The Royal Society, 1997. p.2161-2184.

[40] A.C. Cocks, S.P. Gill, J. Pan, Modeling microstructure evolution in engineering materials. Modeling microstructure evolution in engineering materials 1998;36:81-162.

[41] D. Bouvard, R. McMeeking, Deformation of Interparticle Necks by Diffusion - Controlled Creep. Journal of the American Ceramic Society 1996;79:666-672.

[42] W. Coblenz, J. Dynys, R. Cannon, R. Coble, Initial stage solid state sintering models. A critical analysis and assessment. Initial stage solid state sintering models. A critical analysis and assessment 1980;13:141-157.

[43] W. Zhang, J. Schneibel, The sintering of two particles by surface and grain boundary diffusion—a two-dimensional numerical study. A diffusional creep law for powder compacts 1995;43:4377-4386.

[44] W.D. Kingery, Regelation, Surface Diffusion, and Ice Sintering. Journal of Applied Physics 1960;31:833.

[45] F.A. Nichols, W.W. Mullins, Morphological Changes of a Surface of Revolution due to Capillarity-Induced Surface Diffusion. Journal of Applied Physics 1965;36:1826.

[46] J.G.R. Rockland, On the rate equation for sintering by surface diffusion. Acta Metallurgica 1966;14:1273-1279.

[47] M.C. Iordache, S.H. Whang, Z. Jiao, Z.M. Wang, Grain growth kinetics in nanostructured nickel. Nanostructured Materials 1999;11:1343-1349.

[48] V. Randle, P.R. Rios, Y. Hu, Grain growth and twinning in nickel. Scripta Materialia 2008;58:130-133.

[49] H.V. Atkinson, Overview no. 65: Theories of normal grain growth in pure single phase systems. Acta Metallurgica 1988;36:469-491.

[50] C.E. Krill Iii, L.Q. Chen, Computer simulation of 3-D grain growth using a phase-field model. Acta Materialia 2002;50:3059-3075.

[51] P. Knauth, A. Charaï, P. Gas, Grain growth of pure nickel and of a Ni-Si solid solution studied by differential scanning calorimetry on nanometer-sized crystals. Scripta Metallurgica et Materialia 1993;28:325-330.

[52] J. Wurst, J. Nelson, Lineal Intercept Technique for Measuring Grain Size in Two - Phase Polycrystalline Ceramics. Journal of the American Ceramic Society 1972;55:109-109.

[53] J. Svoboda, H. Riedel, New solutions describing the formation of interparticle necks in solid-state sintering. A diffusional creep law for powder compacts 1995;43:1-10.

[54] R.L. Coble, A Model for Boundary Diffusion Controlled Creep in Polycrystalline Materials. Journal of Applied Physics 1963;34:1679-1682.